Journal of Materials Processing Tech. 354 (2026) 119396

Contents lists available at ScienceDirect

Journal of Materials Processing Tech.

journal homepage: www.elsevier.com/locate/jmatprotec

Short communication

# Absorptivity scaling behaviour during laser powder bed fusion of copper alloys

Sagar Patel [a,*], David Deisenroth [b], Peyman Alimehr [a], Mihaela Vlasea [a,*]

[a] University of Waterloo, Department of Mechanical and Mechatronics Engineering, Waterloo, ON N2L 3G1, Canada
[b] National Institute of Standards and Technology, Gaithersburg, MD, USA

ARTICLE INFO

*Keywords:*
Additive manufacturing
Laser powder bed fusion
Absorptivity scaling
Copper alloys
Laser keyhole
In situ monitoring
Metal powder absorptivity

ABSTRACT

Copper (Cu) and its alloys are used in many industries owing to their high thermal and electrical conductivity, alongside their corrosion resistance and antimicrobial properties. The adoption of Cu-alloys in laser powder bed fusion (PBF-LB) is limited by the high reflectivity of these alloys, particularly at near-infrared wavelengths commonly used in commercial PBF-LB systems. In this work, the absorptivity scaling behaviour of a Cu-alloy (C14500, >99.40% Cu) is characterized using an open-architecture in situ reflectivity measurement setup within an additive manufacturing metrology testbed (AMMT). Reflectivity measurements are taken for 56 process parameter combinations of laser power, velocity, and beam diameter, which capture the range of conduction to keyhole melting modes during PBF-LB of Cu-alloys. Additionally, the absorptivity scaling behaviour for C14500 powder spread on a printed substrate is compared with that of a machined substrate and literature data from calorimetry absorptivity measurements for Ti-, Fe-, and Ni-alloys, to evaluate the effects of substrate roughness and material reflectivity with near-infrared lasers on absorption behaviour in PBF-LB. The results from this work represent a significant advancement in energy coupling physics by demonstrating that the steady-state PBF-LB interactions for copper alloys are governed not only by the intrinsic reflectivity of the material, but also by a surface topography-induced multiple reflections and powder entrainment mechanism. The extreme reflectivity in copper during near-infrared PBF-LB allows for an absorptivity saturation point of 0.91 on printed surfaces and 0.77 on machined surfaces. This distinct behaviour is attributed to the roughness of the printed substrate (which leads to an increased number of scattering events, alongside reduced effects of the Brewster's angle and the realistic powder layer spreading deployed, enhancing the amount of powder particles captured by the melt pool and thereby beam absorption. The measured absorptivity values are analysed using dimensionless parameters, such as normalized enthalpy and diffusion length, to develop an absorptivity scaling equation for PBF-LB of Cu-alloys. This absorptivity scaling equation quantifies laser energy absorption as a function of key PBF-LB parameters and material properties, thereby enhancing predictive capabilities for translation to other Cu-alloys and PBF-LB systems.

## 1. Introduction

The functional properties of copper (Cu) and Cu-alloys, such as its high thermal and electrical conductivity, drive many of its automotive and electrical applications, including radiators, heat exchangers, induction coils, motor components, electrical wiring, electrical switches, and busbars [1]. Cu-alloys also exhibit good corrosion resistance and antimicrobial properties, expanding their areas of application in the medical industry for instruments, plumbing components such as pipes and fittings, construction components such as roofing and gutters, and in marine applications [1].

As shown in literature [2], Cu-based electrical and thermal management devices have been successfully manufactured using conventional manufacturing technologies for numerous applications. However, conventional manufacturing of Cu and Cu-alloys can lead to long lead times from raw material to finished product and limitations in design flexibility [3]. Additive manufacturing (AM) technologies can help offset some of the aforementioned limitations of conventional manufacturing, as well as help expand the applications of Cu and Cu-alloys. For instance, AM of Cu-alloys has the potential to improve performance and manufacturability for applications including windings within electric motors and antennas [4], electrodes for rechargeable batteries [5], electronics packaging [6], and vertical interconnect accesses for the semiconductor and printed circuit board industry [7].

* Corresponding authors.
*E-mail addresses:* sagar.patel@uwaterloo.ca (S. Patel), mihaela.vlasea@uwaterloo.ca (M. Vlasea).

https://doi.org/10.1016/j.jmatprotec.2026.119396
Received 20 January 2026; Received in revised form 19 June 2026; Accepted 20 June 2026
Available online 27 June 2026
0924-0136/

Laser powder bed fusion (PBF-LB/LPBF), also known as selective laser melting (SLM), is an AM technology class that enables near-net-shape fabrication. PBF-LB of Cu and its alloys is of increasing interest due to the potential to fabricate geometries with internal channels and lattice structures, which are particularly useful for applications including but not limited to heat exchangers, conformal cooling channels, and electric motor windings [8]. Additionally, PBF-LB enables the manufacturing of topology-optimized copper components that help reduce weight while maintaining or improving mechanical performance [8].

However, the adoption of PBF-LB Cu and PBF-LB Cu-alloys has been limited by their high reflectivity, particularly at near-infrared wavelengths (≅ 1070 nm), which are commonly used in most commercial PBF-LB systems. The absorptivity of Cu and Cu-alloys at near-infrared wavelengths of lasers is below 5 % in the solid state, and ≅ 15 % in the liquid state [9], and copper powder is shown to have ≅ 33 % absorptivity [10]. This low absorptivity poses challenges for determining processing windows for Cu and its alloys in most PBF-LB systems. Conduction mode melting in PBF-LB, which is typically associated with limited or no vaporization [11], is not sufficient for printing high-density Cu parts [3]. Transition and keyhole mode melting, where significant vaporization is expected, are commonly recommended to increase the laser absorptivity of copper [3]. However, there is a research gap in understanding and modelling the onset of transition and keyhole melting modes during PBF-LB of Cu and its alloys, which makes parameter development for this material class time-intensive and cost-intensive due to trial-and-error approaches [12].

In situ absorptivity measurements of Cu and Cu-alloys under PBF-LB processing conditions are hence essential for understanding laser-material interactions and for rapidly developing parameters for PBF-LB processing. Trapp et al. [13] and Ye et al. [14] have previously performed such measurements for relatively absorptive materials such as Ti, Fe, and Ni alloys. In the work by Ye et al. [14], an absorptivity scaling equation was developed to model absorptivity scaling for this high-absorptivity class of materials and to support both modelling- and experimentally-focused approaches to develop process parameters for these materials. Gargalis et al. [15] used the same approach for PBF-LB of Cu, but experimental limitations (a maximum laser power of 500 W) prevented the derivation of a scaling equation from their results. Nordet et al. [16] used an Ulbricht integrating sphere to measure the absorptivity of Cu during LPBF using a green laser, but most commonly used industrial PBF-LB systems do not use green lasers. It is also commonly assumed that Cu-based powder feedstocks are not easily printable due to their high reflectivity with near-infrared lasers, which drives efforts in creating bespoke Cu-alloys that are specifically geared towards increasing absorptivity [12]. This work challenges this assumption by proving that it is possible to achieve a drastic increase in absorptivity by using the keyhole melting mode during PBF-LB of Cu.

In this work, an in situ PBF-LB reflectivity measurement additive manufacturing metrology testbed (AMMT) was deployed at the National Institute of Standards and Technology (NIST) [17]. The AMMT system was deployed to understand and model, for the first time, the absorptivity scaling behaviour of a Cu-alloy (C14500) with a high Cu-content (> 99.40%). This work addresses two major research questions: (i) is the high reflectivity of Cu and its alloys really detrimental to its printability using near-infrared PBF-LB systems? and (ii) does surface topography influence laser coupling in PBF-LB? By investigating 56 parameter combinations, this work provides proof that the keyhole melting mode in PBF-LB effectively addresses the copper reflectivity challenge by achieving exceptionally high absorptivity values. Additionally, it shows for the first time that in PBF-LB, surface topography has a significant influence on laser absorptivity, with a significant increase in absorptivity observed in rough printed substrates compared to machined substrates. Absorptivity scaling equations are developed for modelling the effects of these roughness differences and melting mode changes as a function of absorptivity during PBF-LB of Cu-alloys.

## 2. Materials and methods

The powder used in this work is pre-alloyed C14500,[1] manufactured by Metal Powder Works (MPW) using a cold mechanically derived process [18], which converts bar stock into powder for additive manufacturing. The composition of the C14500 powder batch was 99.4% copper (Cu), 0.5% tellurium (Te), and 0.1% phosphorus (P). The morphology of the C14500 powder particles used in this study is shown by the scanning electron microscope (SEM) image in Fig. 1(a). Particle size and morphology analysis was conducted using a vision-based particle size analysis system (Camsizer X2, Retsch, Haan, Germany), with detailed measurements provided in Table S1 and Fig. S1 of the Supplemental Material. The powder particles had a D10 of 33 μm, a D50 of 47 μm, and a D90 of 63 μm, and sphericity between 0.7 and 0.8.

The C14500 substrate, as shown in Fig. 1 (b) and (e), was printed on an EOS additive manufacturing customized machines (AMCM) M290 1 kW PBF-LB system with previously developed parameters at a 30 μm layer thickness that led to high-density parts (micrographs of 10-mm edge length cubes showcasing high-density parts are given in Figs. S2 and S3 of the Supplemental Material). The printed C14500 substrate was then placed in the sample well of the NIST AMMT [19,20], with visuals of the system and schematics given in Fig. 1 (d). The laser in the AMMT has a wavelength of 1070 nm. In the metrology mode of the NIST AMMT, the processing area of the AMMT is contained within an integrating hemisphere that allows for understanding laser coupling behaviour in PBF-LB experiments. The integrating sphere measures the total reflected laser power, and the laser coupling value is $A_{lc} = 1 - P_\rho / P$ (where $P_\rho$ is the reflected power and $P$ is the applied laser power). Therefore, it should be noted that this laser coupling measurement is an indirect (inferred) measurement of absorptivity. The term "absorptivity" will be in lieu of "laser coupling" in this paper.

For absorptivity assessments on the C14500 substrate, 56 process parameter combinations were tested, which include a laser power range of 300 W to 600 W in 50 W increments, a velocity range of 300 mm/s to 700 mm/s in 100 mm/s increments, and a beam diameter of 45 μm (focused beam) and 80 μm (defocused divergent beam). Three 10 mm long hatch lines were scanned in alternating anti-parallel directions for each process parameter combination with a hatch distance of 100 μm.

In PBF-LB, measured and predicted powder layer thickness values in the literature are typically much larger than the nominal powder layer thickness values that a user provides as a printing parameter. This is because, after dozens of re-coated layers, an equilibrium thickness is reached that is significantly thicker than the build plate step distance between re-coating cycles. Mahmoodkhani et al. [21] report a measured layer thickness between 6x to 8x the nominal layer thickness, Wischeropp et al. [22] report a measured layer thickness between 4x to 5.5x the nominal layer thickness, and Liu et al. [23] report a measured layer thickness of about 4x the nominal layer thickness. After aligning the top of the samples with the recoater, a powder layer thickness setting of 120 μm was used for these single layer experiments to simulate the steady state powder depth for a nominal 30 μm layer thickness in a commercial PBF-LB system. Half of the 56 parameter combinations were also tested on a machined pure copper substrate, depicted in Fig. 1 (c), with the same three line hatch strategy and a powder layer thickness of 120 μm. Furthermore, 13 parameter combinations from the same range were tested on a machined pure copper substrate with the same hatching strategy, but with no powder spread onto the

[1] Certain equipment, instruments, software, or materials, commercial or non-commercial, are identified in this paper in order to specify the experimental procedure adequately. Such identification does not imply recommendation or endorsement of any product or service by NIST, nor does it imply that the materials or equipment identified are necessarily the best available for the purpose.

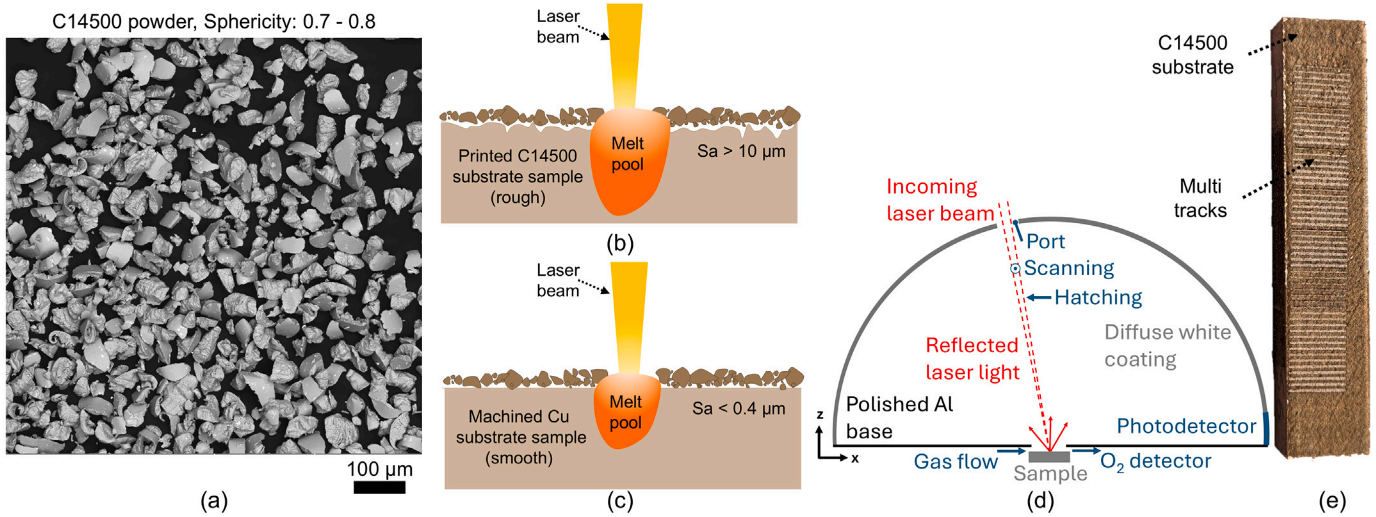


**Fig. 1.** (a) Scanning electron microscope (SEM) image of the Cu alloy (C14500)powder used in this study, (b) schematic of melt pool formation with C14500 powder spread on a printed substrate, (c) schematic of melt pool formation with C14500 powder spread on a machined substrate, (d) laser coupling apparatus schematic and visual of the NIST additive manufacturing metrology testbed (AMMT), (e) C14500 multi-tracks printed on previously printed C14500 substrate (substrate was printed on an EOS AMCM M290 1 kW system).

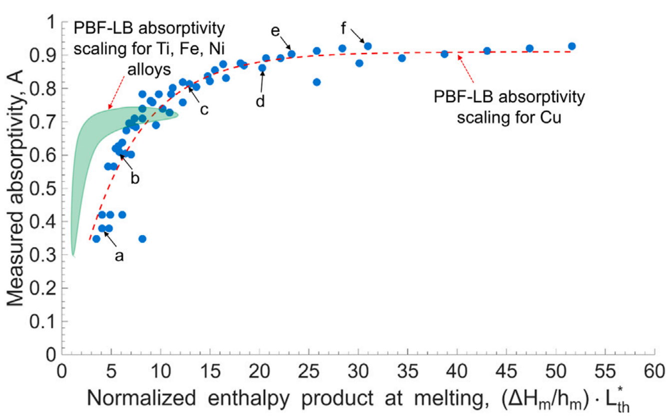


**Fig. 2.** Inferred absorptivity as a function of normalized enthalpy product at melting, $\Delta H_m/h_m \cdot L^*_{th}$, for 56 laser powder bed fusion (PBF-LB)parameter combinations on a copper alloy, C14500. The dotted red line is a curve fitted to all data points, modelled in Eq. 2, with $R^2 = 0.99$. Absorptivity data for a titanium alloy (Ti6Al4V), ferrous alloy (SS 316L), and nickel alloy (IN 625) are shown in the green region and taken from work by Ye et al. [14]. Melt pools from points labelled a to f are shown in Fig. 3.

substrate. The machined substrates were measured to have a surface roughness of Ra = 0.4 μm. Raw data from the absorptivity experiments are provided in Tables S2, S3, and S4in the Supplemental Material. To visualize melt pools from some of the representative datasets, the printed C14500 substrate was sectioned, polished, and etched with ferric chloride etchant.

## 3. Results and discussion

### 3.1. Empirical absorptivity scaling and modelling

Fig. 2 illustrates the inferred laser absorptivity estimates based on results from the C14500 printed substrate experiments against normalized enthalpy product at melting, $\Delta H_m/h_m \cdot L^*_{th}$. Normalized diffusion length, $L^*_{th}$, given by Eq. (2), is derived by Ye et al. [14], which helps to characterize the scale of heat diffusion as a function of the laser beam size. Normalized enthalpy is defined as the ratio of the absorbed energy density to the enthalpy at melting, as defined by King et al. [24]. Normalized enthalpy at melting, as given by Eq. (1), uses the minimum absorptivity value, $A_m$, that we measured in our machined substrate experiments with no powder, which was 0.17 (which we assume to be the absorptivity of copper at melting, and is close to the ≅ 0.15 absorptivity observed for liquid Cu in literature [9]). In Eq. (1) and (2), $P$ is laser power $[W]$, $v$ is beam velocity [ m/s], $r_b$ is beam radius $[m]$, $\rho$ is density of C14500 - 8940 $kg/m^3$ [25], $C_p$ is specific heat capacity - 385 $J/(kg \cdot K)$ [25], $\alpha$ is thermal diffusivity $[m^2/s]$ - calculated by $\lambda/(\rho \cdot C_p)$, where $\lambda$ is thermal conductivity - 355 $W/(m \cdot K)$ [25], $T_m$ is melting/liquidus temperature - 1348 $K$ [25], $T_0$ is the powder bed temperature (which is room temperature for this work, 293 $K$).

$$\frac{\Delta H_m}{h_m} = \frac{A_m P}{\pi \rho C_p (T_m - T_0)\sqrt{\alpha v r_b^3}} \quad (1)$$

$$L^*_{th} = \sqrt{\frac{\alpha}{v r_b}} \quad (2)$$

$$A = 0.91(1 - e^{-0.17(\Delta H_m/h_m)\cdot L^*_{th}}) \quad (3)$$

It is observed that all the measurements collapse onto a single curve that can be modelled by an asymptotic exponential fitting curve, as shown in Fig. 2, and captured in Eq. (3). MATLAB's Curve Fitting Toolbox is used to model the curve in Eq. (3) using the Levenberg–Marquardt/least absolute residuals robust fitting algorithm. The coefficients in Eq. (3) with their 95 % confidence bounds are $0.91^{+0.004}_{-0.013}$ and $0.17^{+0.001}_{-0.009}$. Fig. 2 also includes the ranges of absorptivity data for low reflectivity and low thermal diffusivity materials, such as Ti-alloys (Ti6Al4V), Fe-alloys (stainless steel 316L) and Ni-alloys (nickel super alloy 625), obtained from work by Ye et al. [14]. Melt pools from points labelled a to f in Fig. 2 are shown in Fig. 3, along with their corresponding power, velocity, and beam radius values. Melt pool morphologies from Fig. 3 help validate that the process parameter and absorptivity ranges capture the spectrum of conduction to keyhole melting modes for PBF-LB of C14500. Points a and b from Fig. 3 show conduction mode melt pools with melt pool aspect ratios (defined as the melt pool depth-to-width ratio) below 0.5; points d, e, and f show keyhole mode melt pools with melt pool aspect ratios over 0.8, and point c shows melt pools that would be expected in the transition melting mode, with a melt pool aspect ratio of approximately 0.7 [11]. Keyhole mode melt pools (d, e, and f) cause an increased amount of metal vapour when compared to conduction mode melt pools. This leads to a low-pressure

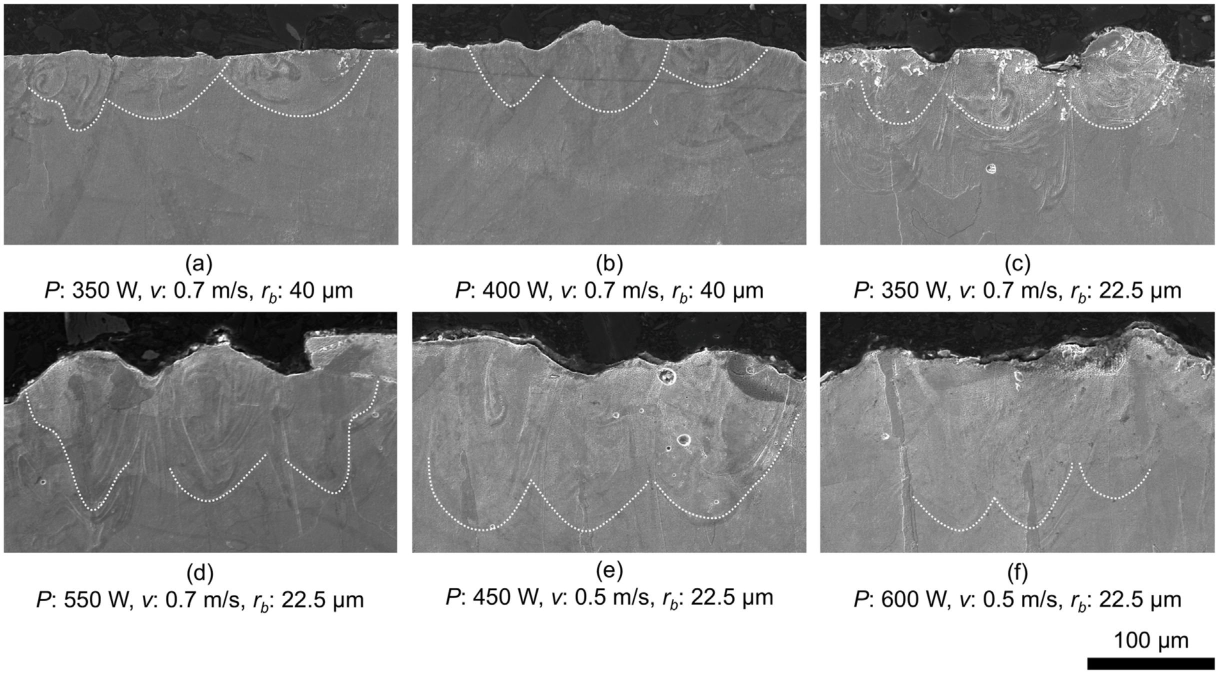


**Fig. 3.** Scanning electron microscope (SEM) images with melt pool boundaries highlighted in dotted white lines for multi-tracks from points labelled (a) to (f) in Fig. 2. Below each micrograph, its laser powder bed fusion (PBF-LB) processing parameters of laser power $P$, beam velocity $v$, and beam radius $r_b$ are provided.

zone near the melt pool caused by the high-speed metal vapour flux, in relation to the surrounding inert (Argon) gas flow which is at a higher pressure. This pressure difference results in a Bernoulli effect-driven entrainment of metal powder particles from the surrounding powder bed [26]. The effect of this increased powder entrainment is observed through a greater melt pool height for the keyhole mode melt pools and a rougher surface. Huang et al. [27] correlate the dimensionless normalized enthalpy product variable (used in this work) with the front vaporized cavity/keyhole wall angle for Ti-, Fe-, Ni-, and Al-alloys. Correlating absorptivity with the front keyhole wall angle would require additional analysis and is outside the scope of this work; an increase in laser absorptivity would be expected to directly correlate to an increase in the vaporized cavity/keyhole penetration depth.

### 3.2. Absorptivity differences in current work compared to literature

The absorptivity scaling behaviour for this Cu alloy is observed to be significantly different from that of low reflectivity materials, such as Ti-, Fe-, and Ni-alloys, in two main ways. First, the normalized enthalpy product at melting values for the conduction and keyhole melting modes in Cu alloys is significantly higher than that of low reflectivity materials, which can be attributed to the considerably higher thermal diffusivity of Cu alloys ($\cong$ 1.03 $cm^2/s$) when compared to Ti-, Fe-, and Ni-alloys (0.048 $cm^2/s$ to 0.086 $cm^2/s$) [14]. Secondly, the absorptivity for Ti-, Fe-, and Ni-alloys in the work by Ye et al. [14] saturates at $\cong$ 0.7, compared to the Cu-alloy used in this work, wherein absorptivity saturates at $\cong$ 0.9 in Fig. 2. One significant difference in the experimental approaches is that the absorptivity data for Cu from Fig. 2 is taken from powder spread on a printed substrate, compared to powder being spread on a machined substrate as done in the work by Ye et al. [14]. Additionally, a steel razor blade was used to spread a 100 µm thick powder layer, which was defined by the rim thickness of precision-machined cups in absorptivity work for Ti-, Fe-, and Ni-alloys, which may lead to a different powder bed density compared to this work [13,14]. The calorimetry methodology used in the work for Ti-, Fe-, and Ni-alloys [13,14] have limitations in their selected range of process parameters (maximum laser power of 300 W, minimum beam spot diameter of 57 µm, and minimum velocity of 500 mm/s) and uncertainty in the results, as a maximum absorptivity of $\cong$ 0.9 has bee reported by Deisenroth et al. [20] using a similar instrumentation as the one used in this work for a Ni-alloy. Similarly, Simonds et al. [28] have reported a maximum absorptivity of $\cong$ 0.85 for a Ti-alloy using integration sphere radiometry. The methodology by Deisenroth et al. [20] has the added benefit of combining reflectometry, calorimetry, and mass loss measurements to capture the reflected energy, absorbed energy, and energy transfer by vaporization. Since the total energy measurements in the work by Deisenroth et al. [20] are shown to sum up to $\cong$ 100 %, it could be assumed that it is possible to achieve $\cong$ 0.9 absorptivity in Ti-, Fe-, and Ni-alloys as well. While calorimetry primarily records the energy converted into heat within the metal, the integrating hemisphere approach used in this work accounts for all energy not reflected back to the source. The maximum absorptivity of $\cong$ 0.9 in this work matches the maximum absorptivity measured by Nordet et al. [16] during PBF-LB of copper in keyhole mode using a green laser, which helps confirm that our process parameter selection range spans the entire spectrum of conduction to keyhole mode melting during PBF-LB of copper.

### 3.3. Surface roughness driven changes in absorptivity scaling behaviour

The difference in absorption behaviour with a change of substrate becomes apparent in Fig. 4, wherein absorptivity scaling behaviour for C14500 is compared for a printed as well as on a machined substrate alongside Ti-, Fe-, and Ni-alloy data obtained from a machined substrate [13,14]. The absorptivity behaviour for C14500 spread on a machined substrate from Fig. 4 is modelled using the same approach as the one used for a printed substrate and is shown in Eq. (4). The coefficients in Eq. (4) with their 95 % confidence bounds are $0.77^{+0.046}_{-0.041}$ and $0.20^{+0.046}_{-0.037}$. When a machined substrate is used for Cu, the absorptivity saturates at $\cong$ 0.77 (with a maximum value of 0.82). A machined/milled substrate typically has a roughness < 0.5 µm, compared to as built top surfaces in PBF-LB that are expected to have roughness > 10 µm [29]. The surface roughness of the printed substrate used in this study was measured using a laser profilometer to be 14 µm.

$$A = 0.77(1 - e^{-0.20(\Delta H_m/h_m)\cdot L_{th}^{*}}) \tag{4}$$

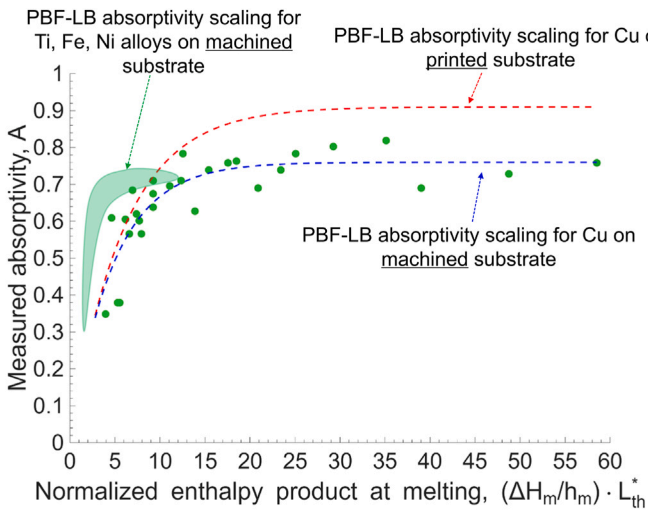


**Fig. 4.** Absorptivity as a function of normalized enthalpy product at melting, $\Delta H_m/h_m \cdot L_{th}^*$, for a Cu alloy (C14500) on a printed and machine substrate, compared to Ti-, Fe-, and Ni-alloys on a machined substrate. Absorptivity data for Ti-, Fe-, and Ni-alloys are shown in the green region, and taken from work by Ye et al. [14].

Studies by Deng et al. [30] and Wu et al. [31] have shown roughness of the substrate/previous layer influences powder spreading behaviour. The roughness of the spread powder layer, combined with the higher roughness of the printed substrate, would help increase powder particles captured by the melt pool (also known as powder entrainment) [13], thereby increasing beam absorption. Using two-dimensional (2D) and three-dimensional (3D) ray tracing analysis, Bergström et al. [32,33] have shown that for normally incident light, $\theta_0 = 0°$, and small angles of incidence (expected in typical industrial PBF-LB systems), the absorptivity of a surface increases with roughness, due to an increase in the average number of scattering events, as shown for smooth machined and rough printed substrate conditions in Fig. 5. The effect of roughness on absorptivity is reduced only at angles of incidence that are 60° and above, which might be the case only for the corners of large-format PBF-LB systems. Their work [32] has also shown that the increase in absorptivity with roughness is most pronounced in materials like copper and aluminium alloys, which have a low absorptivity in the flat, smooth state, compared to Ti-, Fe-, and Ni-alloys. This difference in behaviour is associated with “diminishing returns” when comparing multiple reflections from high and low absorptivity interactions. Assuming smooth and flat surfaces, laser absorptivity is shown to increase significantly (followed by a dramatic drop) around Brewster’s maximum angle in PBF-LB [27], and laser powder fed AM literature [34], and depicted by the absorptivity increase followed by a dramatic drop for machined substrates around $\theta_0 = 85°$ in Fig. 5. $\sigma$ is the root mean square (RMS) roughness and $\tau$ is the surface correlation length in Fig. 5, as described by Bergström et al. [32]. $\sigma/\tau$ values of 0.5 to 2.0, considered as rough surfaces by Bergström et al. [32] are assumed to be comparable to the printed PBF-LB substrate boundary conditions. For the machined substrate boundary condition, a smooth surface with a low $\sigma/\tau$ value of about 0.01 is assumed, wherein the absorptivity behaviour is similar to the theoretical Fresnel absorptivity curve in Fig. 5. Bergström et al. [32,33] have shown that for rough surfaces, the effect of Brewster’s angle in terms of a dramatic drop in absorptivity is eliminated, and this would mean a higher absorption of laser reflections that is independent of its angle of incidence as depicted by the absorptivity versus angle of incidence, $\theta_0$, plot for printed substrates in Fig. 5. This means that for high reflectivity materials like copper and aluminium alloys, laser absorption is consistently higher for rough surfaces at all angles except in the vicinity of Brewster’s angle, i.e., between 75° and 85°. Past the Brewster’s angle (above 85°), the laser absorptance of rough surfaces in these alloys would still stay consistent when compared to an absorptivity drop to nearly 0 for smooth surfaces.

While the SEM images of the cold mechanically derived powders may appear unique and unconventional, they have been used to obtain high-density Al parts using PBF-LB in prior literature [18,35], which can achieve equivalent properties to wrought materials [18]. Using the same batch of C14500 powder (as the one used for the absorptivity study), the authors are also able to obtain near-full-density parts using keyhole mode parameters, as shown by micrographs in Fig. S2 and Fig. S3 of the Supplemental Material. A time-lapse video of a print using MPW’s C14500 powder on an EOS M290 1 kW PBF-LB system is provided in the Supplementary Video; the video is from a print consisting of sixteen gears with a diameter of 58 mm and a height of 7.5 mm. The unique morphology of cold mechanically derived powders, compared to atomized powders commonly used in PBF-LB, may affect the initial laser absorption behaviour before a stable melt pool is established. However, the effects of the powder morphology and/or size would be minimal on steady-state melt pools when compared to the effects of the actual melting modes of the melt pools [36].

This research provides multiple first-time proofs that would be vital for the additive manufacturing community. Most notably, this work has successfully understood and modelled the absorptivity scaling behaviour for a high copper content copper alloy using a realistic powder on printed substrate experiment. This is an important departure from previous studies that relied on machined surfaces, which do not accurately reflect the conditions within an industrial PBF-LB build. Additionally, this work shows that the absorptivity of copper using a near-infrared wavelength laser can reach a saturation point of 0.9 (90 %) when processed on a printed substrate.

The derived absorptivity scaling equation can replace the need for assuming a constant absorptivity value, which is often a major source of error in analytical [37] and numerical [38] PBF-LB simulations. Additionally, the scaling equation allows for the creation of process maps that can translate parameters across different PBF-LB systems. For instance, if we know the material properties for a given copper alloy and the beam diameter of a given PBF-LB system, we can use the scaling law to predict the required power and speed to achieve a particular melting mode.

## 4. Conclusions

Absorptivity scaling behaviour during laser powder bed fusion (PBF-LB) of a Cu alloy was characterized as a function of key process parameters, including laser power, velocity, and beam radius, spanning across melting modes. This work provides experimental proof that the keyhole melting mode effectively flips the copper reflectivity challenge by measurements of > 90 % absorptivity, higher than those for any other material reported in near-infrared PBF-LB literature. Absorptivity during PBF-LB of Cu also scales significantly differently when compared to low reflectivity and low diffusivity materials such as Ti-, Fe-, and Ni-alloys. Absorptivity during PBF-LB of Cu saturates at ≅ 0.9 on a printed substrate and ≅ 0.77 on a machined substrate, compared to a maximum of ≅ 0.7 observed using calorimetry measurements during PBF-LB of Ti-, Fe-, and Ni-alloys on a machined substrate. Additionally, it shows for the first time that in PBF-LB, surface topography has a significant influence on laser coupling, with an increase of ≅15 % absorptivity observed in printed substrates (roughness, Ra = 14 μm) compared to machined substrates (Ra = 0.4 μm). This increase is attributed to multiple factors, including an increased number of scattering events and reduced effects of the Brewster’s angle.

Lastly, analytical absorptivity scaling equations are developed wherein absorptivity is a function of the normalized enthalpy at melting and the normalized diffusion length for PBF-LB of Cu using both printed and machined substrates. These equations help to understand and model

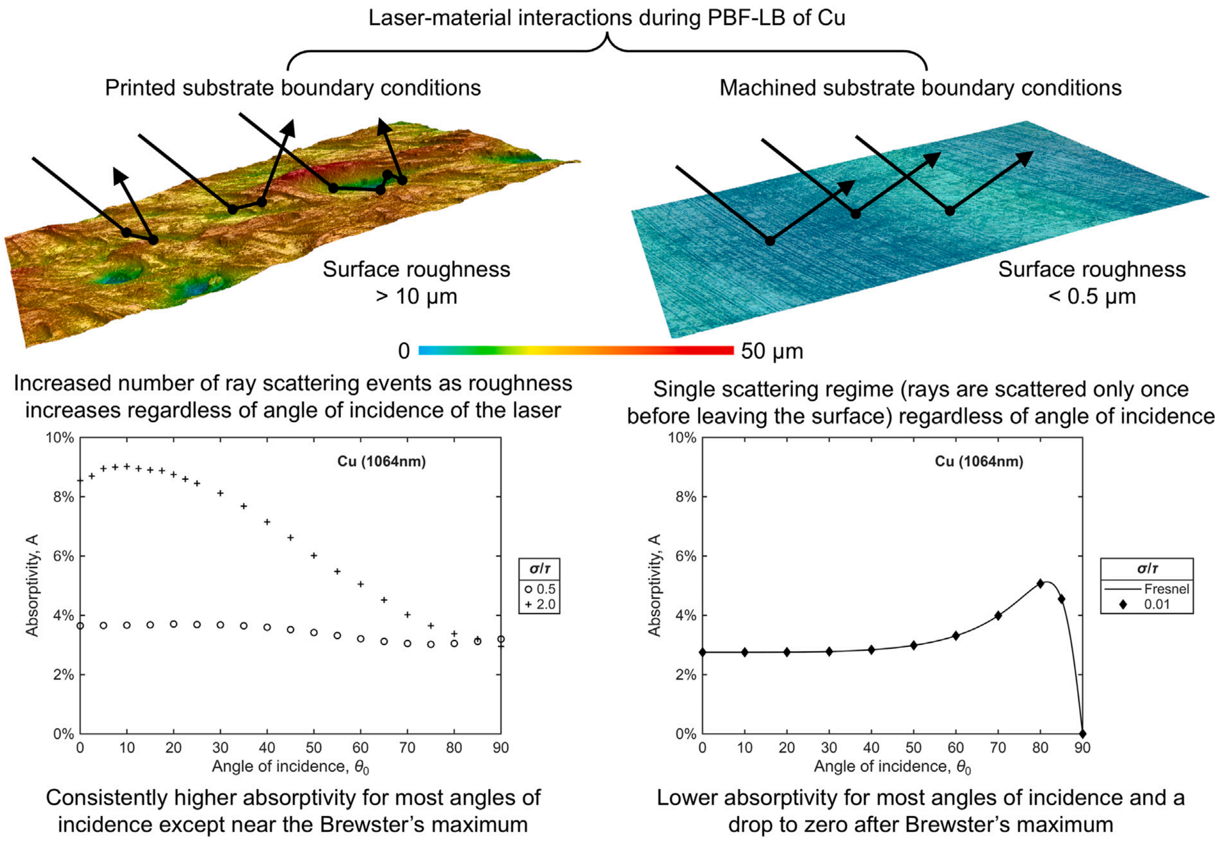


**Fig. 5.** Illustrative diagram of laser material interactions during PBF-LB of Cu comparing printed and machined surface boundary conditions. Multiple ray scattering events are expected in printed substrates with higher roughness when compared to smooth machined substrates. Absorptivity versus angle of incidence for pure copper at a laser wavelength of 1064 nm is plotted for rough and smooth substrate boundary conditions using ray tracing simulation results from Bergström et al. [32]. $\sigma/\tau$ of 0.5 to 2.0 corresponds to a rough printed surface condition, wherein $\sigma$ is the root mean square (RMS) roughness and $\tau$ is the surface correlation length. Machined substrates would correspond to a low $\sigma/\tau$ value of 0.01, which is close to the Fresnel absorptivity curve for Cu.

the effects of roughness differences and melting modes changes as a function of absorptivity during PBF-LB of Cu-alloys with near-infrared lasers.

Findings from this work help alleviate common concerns about the absorptivity of Cu and its alloys using near-infrared PBF-LB systems, especially with absorptivities greater than 90 % possible in the keyhole melting mode. Additionally, the positive effect of higher surface roughness on absorption can aid AM practitioners in planning for the PBF-LB processing of similar high reflectivity materials (e.g. aluminium or silver alloys). Lastly, the analytical expression derived in the work for PBF-LB of Cu can also aid the development of computationally efficient temperature models. Future work would include modelling the specific effects of surface roughness on absorptivity using physics-based approaches, alongside modelling the relationship between PBF-LB absorptivity and front keyhole wall angle for Cu and other materials.

## CRediT authorship contribution statement

**Sagar Patel:** Writing – review & editing, Writing – original draft, Visualization, Validation, Software, Methodology, Investigation, Formal analysis, Data curation, Conceptualization. **David Deisenroth:** Writing – review & editing, Validation, Methodology, Investigation. **Peyman Alimehr:** Visualization, Methodology, Data curation. **Mihaela Vlasea:** Writing – review & editing, Supervision, Resources, Project administration, Methodology, Funding acquisition, Conceptualization.

## Declaration of competing interest

The authors declare that they have no known competing financial interests or personal relationships that could have appeared to influence the work reported in this paper.

## Acknowledgements

The authors would like to thank Metal Powder Works (Pittsburgh, PA, USA) for providing the powders used in this study. Additionally, Sagar Patel, Peyman Alimehr, and Mihaela Vlasea appreciate the funding support received from the Federal Economic Development Agency for Southern Ontario, Regional Innovation Ecosystem, Canada (FedDev Ontario project number 1016969). David Deisenroth's work was funded by the United States Government through NIST.

## Appendix A. Supplementary data

Supplementary material related to this article can be found online at https://doi.org/10.1016/j.jmatprotec.2026.119396.

## References

[1] P. Robinson, Applications of copper and copper alloys, in: Properties and Selection: Nonferrous Alloys and Special-Purpose Materials, vol. 2, ASM International, 1990, pp. 239–240, http://dx.doi.org/10.31399/asm.hb.v02.a0001067.

[2] R. Caron, Copper alloys: Properties and applications, in: Encyclopedia of Materials - Science and Technology, vol. 1, Elsevier, 2001, pp. 1665–1668, http://dx.doi.org/10.1016/B0-08-043152-6/00292-8.

[3] S.D. Jadhav, L.R. Goossens, Y. Kinds, B.V. Hooreweder, K. Vanmeensel, Laser-based powder bed fusion additive manufacturing of pure copper, Addit. Manuf. 42 (2021) 101990, http://dx.doi.org/10.1016/j.addma.2021.101990.
[4] D. Schuhmann, C. Rockinger, M. Merkel, D.K. Harrison, A study on additive manufacturing for electromobility, World Electr. Veh. J. 13 (8) (2022) http://dx.doi.org/10.3390/wevj13080154.
[5] P. Nyamekye, P. Nieminen, M.R. Bilesan, E. Repo, H. Piili, A. Salminen, Prospects for laser based powder bed fusion in the manufacturing of metal electrodes: A review, Appl. Mater. Today 23 (2021) 101040, http://dx.doi.org/10.1016/j.apmt.2021.101040.
[6] R.I. Olivas, Conformal Electronics Packaging through Additive Manufacturing and Micro-Dispensing (Ph.D. thesis), The University of Texas at El Paso, Texas, USA, 2011, URL https://www.proquest.com/docview/874289503/abstract/8A5A9DFB235B469DPQ/1.
[7] L. Overmeyer, E. Olsen, G.-A. Hoffmann, Additive manufacturing of copper vertical interconnect accesses by laser processing, CIRP Ann 70 (1) (2021) 163–166, http://dx.doi.org/10.1016/j.cirp.2021.03.006.
[8] J.N. Orakwe, S.I. Shahabad, O. Ibhadode, A. Bonakdar, E. Toyserkani, An integration of topology optimization and conformal minimal surfaces for additively manufactured liquid-cooled heat sinks, Addit. Manuf. 107 (2025) 104814, http://dx.doi.org/10.1016/j.addma.2025.104814.
[9] M. Roccetti Campagnoli, M. Galati, A. Saboori, On the processability of copper components via powder-based additive manufacturing processes: Potentials, challenges and feasible solutions, J. Manuf. Process. 72 (2021) 320–337, http://dx.doi.org/10.1016/j.jmapro.2021.10.038.
[10] A. Domine, C. Verdy, C. Penaud, L. Vitu, N. Fenineche, L. Dembinski, Selective laser melting (SLM) of pure copper using 515-nm green laser: From single track analysis to mechanical and electrical characterization, Int. J. Adv. Manuf. Technol. (2023) http://dx.doi.org/10.1007/s00170-023-12338-5.
[11] S. Patel, M. Vlasea, Melting modes in laser powder bed fusion, Materialia 9 (2020) 100591, http://dx.doi.org/10.1016/j.mtla.2020.100591.
[12] B. Bhatt, A. Martucci, S. Biamino, D. Ugues, F. Bondioli, L. Montanaro, M. Lombardi, P. Fino, Current trends in electron beam and laser powder bed fusion additive manufacturing of copper alloys: Composition, defects, properties, and challenges, Mater. Des. 253 (2025) 113742, http://dx.doi.org/10.1016/j.matdes.2025.113742.
[13] J. Trapp, A.M. Rubenchik, G. Guss, M.J. Matthews, In situ absorptivity measurements of metallic powders during laser powder-bed fusion additive manufacturing, Appl. Mater. Today 9 (2017) 341–349, http://dx.doi.org/10.1016/j.apmt.2017.08.006.
[14] J. Ye, S.A. Khairallah, A.M. Rubenchik, M.F. Crumb, G. Guss, J. Belak, M.J. Matthews, Energy Coupling Mechanisms and Scaling Behavior Associated with Laser Powder Bed Fusion Additive Manufacturing, Adv. Eng. Mater. 21 (7) (2019) 1900185, http://dx.doi.org/10.1002/adem.201900185.
[15] L. Gargalis, J. Ye, M. Strantza, A. Rubenchik, J.W. Murray, A.T. Clare, I.A. Ashcroft, R. Hague, M.J. Matthews, Determining processing behaviour of pure Cu in laser powder bed fusion using direct micro-calorimetry, J. Mater. Process. Technol. 294 (2021) 117130, http://dx.doi.org/10.1016/j.jmatprotec.2021.117130.
[16] G. Nordet, C. Gorny, Y. Mayi, J. Daligault, M. Dal, A. Effernelli, E. Blanchet, F. Coste, P. Peyre, Absorptivity measurements during laser powder bed fusion of pure copper with a 1 kW cw green laser, Opt. Laser Technol. 147 (2022) 107612, http://dx.doi.org/10.1016/j.optlastec.2021.107612.
[17] B. Lane, S. Mekhontsev, S. Grantham, M.L. Vlasea, J. Whiting, H. Yeung, J. Fox, C. Zarobila, J. Neira, M. McGlauflin, L. Hanssen, S. Moylan, A. Donmez, J. Rice, Design, Developments, and Results from the NIST Additive Manufacturing Metrology Testbed (AMMT), in: 2016 International Solid Freeform Fabrication Symposium, University of Texas at Austin, Austin, TX, 2016, URL https://hdl.handle.net/2152/89662.
[18] J.H. Martin, J.E. Barnes, K.A. Rogers, J. Hundley, D.L. LaPlant, S. Ghanbari, J.-T. Tsai, D.F. Bahr, Additive manufacturing of a high-performance aluminum alloy from cold mechanically derived non-spherical powder, Commun. Mater. 4 (1) (2023) 39, http://dx.doi.org/10.1038/s43246-023-00365-4.
[19] M. Vlasea, B. Lane, F. Lopez, S. Mekhontsev, M. Donmez, Development of powder bed fusion additive manufacturing test bed for enhanced real time process control, in: Solid Freeform Fabrication Symposium, Austin, TX, 2015, pp. 527–539, URL https://hdl.handle.net/2152/89356.
[20] D.C. Deisenroth, S. Mekhontsev, B. Lane, Measurement of mass loss, absorbed energy, and time-resolved reflected power for laser powder bed fusion, in: Laser 3D Manufacturing VII, vol. 11271, SPIE, California, USA, 2020, pp. 46–58, http://dx.doi.org/10.1117/12.2547491.
[21] Y. Mahmoodkhani, U. Ali, S. Imani Shahabad, A. Rani Kasinathan, R. Esmaeilizadeh, A. Keshavarzkermani, E. Marzbanrad, E. Toyserkani, On the measurement of effective powder layer thickness in laser powder-bed fusion additive manufacturing of metals, Prog. Addit. Manuf. 4 (2) (2019) 109–116, http://dx.doi.org/10.1007/s40964-018-0064-0.
[22] T.M. Wischeropp, C. Emmelmann, M. Brandt, A. Pateras, Measurement of actual powder layer height and packing density in a single layer in selective laser melting, Addit. Manuf. 28 (2019) 176–183, http://dx.doi.org/10.1016/j.addma.2019.04.019.
[23] T. Liu, C.S. Lough, H. Sehhat, Y.M. Ren, P.D. Christofides, E.C. Kinzel, M.C. Leu, In-situ infrared thermographic inspection for local powder layer thickness measurement in laser powder bed fusion, Addit. Manuf. 55 (2022) 102873, http://dx.doi.org/10.1016/j.addma.2022.102873.
[24] W.E. King, H.D. Barth, V.M. Castillo, G.F. Gallegos, J.W. Gibbs, D.E. Hahn, C. Kamath, A.M. Rubenchik, Observation of keyhole-mode laser melting in laser powder-bed fusion additive manufacturing, J. Mater. Process. Technol. 214 (12) (2014) 2915–2925, http://dx.doi.org/10.1016/j.jmatprotec.2014.06.005.
[25] P. Robinson, Properties of wrought coppers and copper alloys, in: Properties and Selection: Nonferrous Alloys and Special-Purpose Materials, vol. 2, ASM International, 1990, pp. 265–279, http://dx.doi.org/10.31399/asm.hb.v02.a0001067.
[26] M.J. Matthews, G. Guss, S.A. Khairallah, A.M. Rubenchik, P.J. Depond, W.E. King, Denudation of metal powder layers in laser powder bed fusion processes, Acta Mater. 114 (2016) 33–42, http://dx.doi.org/10.1016/j.actamat.2016.05.017.
[27] Y. Huang, T.G. Fleming, S.J. Clark, S. Marussi, K. Fezzaa, J. Thiyagalingam, C.L.A. Leung, P.D. Lee, Keyhole fluctuation and pore formation mechanisms during laser powder bed fusion additive manufacturing, Nat. Commun. 13 (1) (2022) 1170, http://dx.doi.org/10.1038/s41467-022-28694-x.
[28] B.J. Simonds, J. Tanner, A. Artusio-Glimpse, P.A. Williams, N. Parab, C. Zhao, T. Sun, The causal relationship between melt pool geometry and energy absorption measured in real time during laser-based manufacturing, Appl. Mater. Today 23 (2021) 101049, http://dx.doi.org/10.1016/j.apmt.2021.101049.
[29] A. Fortunato, A. Lulaj, S. Melkote, E. Liverani, A. Ascari, D. Umbrello, Milling of maraging steel components produced by selective laser melting, Int. J. Adv. Manuf. Technol. 94 (5) (2018) 1895–1902, http://dx.doi.org/10.1007/s00170-017-0922-9.
[30] Y. Deng, Z. Sang, J. Zhang, F. Radtke, L. Becker, S. Herzog, S. Weber, C. Broeckmann, Numerical studies of influencing factors on the homogeneity of the powder mixture during the powder spreading process of powder bed fusion–laser beam/metal, Adv. Eng. Mater. 27 (14) (2025) 2400305, http://dx.doi.org/10.1002/adem.202400305.
[31] Y. Wu, F. Chu, C. Zhang, H. Yan, L. Wang, Z. Zhou, Influence of substrate surface morphology on powder spreading in laser powder bed fusion process, Powder Technol. 464 (2025) 121296, http://dx.doi.org/10.1016/j.powtec.2025.121296.
[32] D. Bergström, J. Powell, A.F.H. Kaplan, A ray-tracing analysis of the absorption of light by smooth and rough metal surfaces, J. Appl. Phys. 101 (11) (2007) 113504, http://dx.doi.org/10.1063/1.2738417.
[33] D. Bergström, J. Powell, A.F. Kaplan, The absorption of light by rough metal surfaces—A three-dimensional ray-tracing analysis, J. Appl. Phys. 103 (10) (2008) 103515, http://dx.doi.org/10.1063/1.2930808.
[34] Y. Huang, M.B. Khamesee, E. Toyserkani, A comprehensive analytical model for laser powder-fed additive manufacturing, Addit. Manuf. 12 (2016) 90–99, http://dx.doi.org/10.1016/j.addma.2016.07.001.
[35] A. Rezaei, M.K. Keshavarz, J. Barnes, M. Vlasea, Melting mode-driven processing diagram for nanoparticle-enhanced high-strength aluminum alloy processed by laser powder bed fusion, Mater. Des. 252 (2025) 113794, http://dx.doi.org/10.1016/j.matdes.2025.113794.
[36] A. Aggarwal, Y.C. Shin, A. Kumar, Investigation of the transient coupling between the dynamic laser beam absorptance and the melt pool - vapor depression morphology in laser powder bed fusion process, Int. J. Heat Mass Transfer 201 (2023) 123663, http://dx.doi.org/10.1016/j.ijheatmasstransfer.2022.123663.
[37] W. Wang, J. Ning, H. Garmestani, S.Y. Liang, Analytical prediction of molten pool dimensions in powder bed fusion considering process conditions-dependent laser absorptivity, Appl. Sci. 12 (23) (2022) http://dx.doi.org/10.3390/app122311926.
[38] Z. Ren, D.Z. Zhang, G. Fu, J. Jiang, M. Zhao, High-fidelity modelling of selective laser melting copper alloy: Laser reflection behavior and thermal-fluid dynamics, Mater. Des. 207 (2021) 109857, http://dx.doi.org/10.1016/j.matdes.2021.109857.